Chapter 7

Optical Excitations of Colloidal Core/Shell Semiconductor Quantum Dots

Tiberius O. Cheche

Additional information is available at the end of the chapter

http://dx.doi.org/10.5772/65091

Abstract

The energy structure of multi-layer core/shell semiconductor quantum dots (QDs) is simulated and the optical absorption is described within the linear response theory. The lattice-mismatch strain field of the multi-layer nanostructures of spherical symmetry is modelled by a linear continuum elasticity treatment. The excitonic effect is estimated by a configuration interaction approach. Multi-layer core/shell QDs of II-VI semiconductors with heterostructures of type I and II are discussed. Localization of the photo-excited carriers induced by coating explains the optical stability of these multi-layer nanostructures.

Keywords: strain, semiconductor, quantum dot, optical absorption

1. Introduction

Semiconductor quantum dots (QDs) are nanometre-scale objects that are different to the usual optical materials, have size-tuneable and narrow fluorescence and broad absorption spectra. The large interest for these materials comes from their technical applications and theoretical openings. For example, the colloidal multi-shell QDs have led to the development of high-efficiency solar cells [1] or laser applications [2], and probably the most important in the immediate future, to molecular diagnostics and pathology [3]. At theoretical level, the study of magnetism [4] or photon entanglement [5] is an example in which the theoretical studies emerge in promising new properties of electronic devices for spintronics or computer microchips. The main factors used in tuning the physical properties of QDs are the shape and size confinement, and the lattice-mismatch-induced strain. 'Giant' core/multi-shell of 18–19 monolayers (MLs) shell thickness can be prepared with low cost by chemical synthesis [6, 7]. The theoretical

predictions of electronic structures and optical properties are important in the core/shell quantum dots (CSQDs) engineering. Modelling of the lattice-mismatch strain is a key factor in obtaining an accurate physical description of CSQDs. Widely used for analysing the linear elasticity of epitaxial-strained heterointerfaces, the valence force field method (see, e.g. Ref. [8]) has some limitations as the predictions are dependent of *a priori* information regarding the interface structure and surface passivation. There are several theoretical studies of multi-component nanocrystals, in which the role of the strain is considered by *ab-initio* calculations [9–11]. Structural limitations of these first-principle calculations (e.g. band gap underestimation) and also more important, the computational cost for larger QDs, make difficult comparison between theoretical predictions and the experiment. The continuum elasticity approach in the limits of homogeneous and isotropic materials has been shown to be in good agreement with the valence force field models for semiconductor QDs of spherical shape and cubic symmetry (see, e.g. Ref. [12]).

In this context, in this chapter, we discuss optical properties of CSQDs. In Section 2, we introduce the theoretical modelling. In Section 2.1, we describe the lattice-mismatch strain field in core/multi-shell nanostructures by a continuum elasticity approach. In Sections 2.2 and 2.3, we describe the electronic structures and obtain the single-particle states (SPSs) by an effective two-band model and by an eight-band model within the **k·p** theory, respectively. In Section 2.4, we discuss the excitonic effect in QDs. In Section 2.5, the optical absorption coefficient is obtained by taking into account the excitonic effect. In Section 3, we apply the theory presented in the previous section to several types of semiconductor CSQDs with heterostructures of type I and II. Conclusions are presented in Section 4.

2. Theoretical modelling of core/shell semiconductor quantum dots

The theoretical models introduced in this section combine knowledge from classical mechanics, solid state physics and quantum optics for description of elasticity, electronic structure and optical spectra in CSQDs.

2.1. Strain field and the band lineup in the presence of the strain

In the elasticity theory, description of the strain field in finite-domain elastic bodies is a difficult problem. Elaborate solutions for such a problem are obtained in few particular cases for Eshelby-type inclusion of a finite elastic body (see Ref. [13]). In what follows, we introduce an efficient simple method to obtain the strain field in concentric spherical domains of different elastic parameters, which satisfies the necessary accuracy level for our problem. We start by observing that for an elastic spherical core/shell structure, the displacement field, **u**, has radial symmetry and consequently the field is *irrotational*. Within the continuum elasticity approach, the equilibrium equation is grad $div\,\mathbf{u} = 0$ [14]. To obtain the strain field, the linear stress-strain tensor ($\sigma_{ij} - \varepsilon_{ij}$) relation is used. For a structure core/shell/shell (CSS QD) with radii r_1 (for the core), r_2 (for core + middle shell) and R (for the total radius of core + middle shell + outer shell), we consider the following boundary conditions: (a) continuous stress at the interfaces,

http://dx.doi.org/10.5772/65091

(b) zero pressure outside nanostructure and (c) *shrink-fit* induced by the lattice-mismatch. Transposed in algebraic equations, we have

$$\sigma_{rr}^{\mathrm{A}}(r_1) = \sigma_{rr}^{\mathrm{B}}(r_1),\ \sigma_{rr}^{\mathrm{B}}(r_2) = \sigma_{rr}^{\mathrm{C}}(r_2), \tag{1a}$$

$$\sigma_{rr}^{\mathrm{C}}(R) = 0 \tag{1b}$$

$$u_r^A(r_1) - u_r^B(r_1) = \varepsilon_1 r_1,\ u_r^B(r_2) - u_r^C(r_2) = \varepsilon_2 r_2\ , \tag{1c}$$

where $\varepsilon_1 = (a_B - a_A)/a_A$ and $\varepsilon_2 = (a_C - a_B)/a_B$ are relative lattice-mismatches, and *A*, *B* and *C* denote the core, middle and outer shell, respectively. In Eq. (1c), which makes connection between the continuum elastic and the discrete crystalline approaches, a_A, a_B, a_C represent the lattice constants of the crystals. The solutions for the radial displacement in domain *X* (*X* = *A*, *B*, *C*) should respect the above-mentioned equilibrium equation, that in spherical coordinates r, θ, φ are of the form $\boldsymbol{u}_r^X(r) = X_1 r + X_2/r^2$ (with X_1, X_2 as constants). Then, using the spherical coordinates, we derive the strain tensor components from their definition with respect to the displacement. Then, we obtain the stress tensor σ_{ij} in each domain by applying, as mentioned above, the linear stress-strain tensor Hooke's law, $\sigma_{ij} = E(1+\nu)^{-1}\left[\varepsilon_{ij} + \nu(1-2\nu)^{-1}\varepsilon_{ll}\delta_{ij}\right]$ (where *E* is the Young modulus and ν is Poisson ratio). Finally, the constants X_1, X_2 for each domain are found by solving Eqs. (1) and the strain tensor components emerge from their definitions. The values of the hydrostatic strain, $\varepsilon_{hyd} = \varepsilon_{rr} + \varepsilon_{\theta\theta} + \varepsilon_{\varphi\varphi}$ for the case of similar elastic parameters of the three materials, $\nu_A = \nu_B = \nu_C = \nu$, $E_A = E_B = E_C$ are as follows:

$e_{hyd}^A = \alpha\left[\varepsilon_1\left(1 - r_1^3 R^{-3}\right) + \varepsilon_2\left(1 - r_2^3 R^{-3}\right)\right]$, $e_{hyd}^B = \alpha\left[-\varepsilon_1 r_1^3 R^{-3} + \varepsilon_2\left(1 - r_2^3 R^{-3}\right)\right]$, $e_{hyd}^C = -\alpha\left(\varepsilon_1 r_1^3 R^{-3} + \varepsilon_2 r_2^3 R^{-3}\right)$, with $\alpha = 2(1-2\nu)(1-\nu)^{-1}$. One can observe that in the limit of thick outer shell, the outer shell hydrostatic strain vanishes, which is in accordance with the physics anticipation. Complete expressions of the strain tensor components are presented in Ref. [15]. Our expressions for the strain tensor recover the results obtained in Ref. [16] for one shell or those obtained in Ref. [17] for core embedded in an infinite matrix. The method we described can be applied to spherical multi-shell nanostructures and to cylindrical multi-layer structures as well.

The band offset is an important parameter in modelling the physical properties of semiconductor heterostructures. Simple relations are obtained for the band lineup in the presence of the strain for a two-band model within the effective mass approximation. Thus, the energy values at the Γ point of the valence band (VB) and conduction band (CB) for direct band gap semiconductors are given by the equation [18]:

$$E_{v,c} = E_{v,c}^u + a_{v,c}\varepsilon_{hyd}\,, \tag{2}$$

where the unstrained (bulk) values are related by $E_c^u = E_v^u + E_g$ (with E_g, the unstrained (bulk) band gap), and $a_{v(c)}$ is the volume deformation potential (subscript $v(c)$ stands for VB(CB)). Within **k·p** theory, in a multi-band approach, the kinetic and strain Hamiltonians are obtained according to the point group the semiconductors belong. By using a perturbation theory or a group theory-based method (method of invariants), the expressions of the kinetic and strain Hamiltonians are written for the desired number of bands. For example, based on the work of Kane [19] and Bir and Pikus [20], expressions of the eight-band kinetic and strain bulk Hamiltonians, including the spin-orbit interaction for zinc blende crystals, are obtained in Ref. [21]. The multi-band kinetic plus strain Hamiltonians are adapted to limited size structures by adding a cut-off potential (corresponding to a buffer shell), which allows the electron to leak more or less into the environment, outside the structure.

2.2. Single-particle states by two-band model within the effective mass approach

The electron and hole SPSs are obtained by solving the Schrödinger equation for the envelope wave function $H\psi(\mathbf{r}) = E\psi(\mathbf{r})$. The one-band effective Hamiltonian is

$$\left[\frac{p^2}{2\mu(r)} + V(r)\right]\psi(\mathbf{r}) = E\psi(\mathbf{r}), \tag{3}$$

where $\mu(r) = \mu_i$ is the photoexcited (electron or hole) carrier r-dependent effective mass, $V(r) = V_i$ is the step confinement potential generated by the band lineup of the materials in the presence of the strain, as described in Section 2.1, and $i = A, B, C$ for core, middle shell outer shell, respectively. The solution $\psi(\mathbf{r})$ separates in a product of a radial function and spherical harmonics $\psi_{nlm}(\mathbf{r}) = R_l(r)Y_l^m(\theta,\varphi)$, and with $\rho = k_i r$, $R_l(r) = v_l(\rho)$ and $k_i^2 = 2\mu_i\left|E - V_i\right|/\hbar^2$ for the radial one-particle Schrödinger equation, one obtains the spherical Bessel differential equation:

$$\rho^2\frac{d^2v_l(\rho)}{d\rho^2} + 2\rho\frac{dv_l(\rho)}{d\rho} \pm \left[\rho^2 \mp l(l+1)\right]v_l(\rho) = 0, \tag{4}$$

where the upper sign corresponds to $E > V_i$ and the lower to $E < V_i$. Solutions of Eq. (7) are spherical Bessel functions $j_l(\rho), y_l(\rho)$ (upper sign) or modified spherical Bessel functions $i_l(\rho), k_l(\rho)$ (lower sign). The radial wave function for the three regions, A, B, C, are linear combinations of these functions as follows:

$$\begin{cases} R_l^A(r) = A_1^l\, f_{1l}^A(k_A r),\ 0 \le r < r_1 \\ R_l^B(r) = B_1^l\, f_{1l}^B(k_B r) + B_2^l\, f_{2l}^B(k_B r),\ r_1 \le r < r_2 \\ R_l^C(r) = C_1^l\, f_{1l}^C(k_C r) + C_2^l\, f_{2l}^C(k_C r),\ r_2 \le r < R \end{cases}, \tag{5}$$

where A_1^l, $B_{1,2}^l$, $C_{1,2}^l$ are constants and $f_{1l,2l}^{\eta}$ are spherical Bessel functions with the argument dependent of $k_\eta = \hbar^{-1}\sqrt{2m_\eta\left|E - V_\eta\right|}$ $(\eta = A, B, C)$. The functions *f* are chosen according to the resulting band lineup (with taken into account the strain). Imposing the physical conditions of continuity, $R_l^A(r_1) = R_l^B(r_1)$, $R_l^B(r_2) = R_l^C(r_2)$ and $R_l^c(R) = 0$, and conservation of the probability current, $m_A^{-1}\left(dR_l^A/dr\right)_{r\to r_1} = m_B^{-1}\left(dR_l^B/dr\right)_{r\to r_1}$ and $m_B^{-1}\left(dR_l^B/dr\right)_{r\to r_2} = m_C^{-1}\left(dR_l^B/dr\right)_{r\to r_2}$, we obtain the transcendental equation valid for *any* relative position of the band lineup for the three regions:

$$\frac{m_C f_{1l}^B{}'(r_2) - m_B F_l^C f_{1l}^B(r_2)}{m_C f_{2l}^B{}'(r_2) - m_B F_l^C f_{2l}^B(r_2)} = \frac{m_A f_{1l}^A(r_1) f_{1l}^B{}'(r_1) - m_B f_{1l}^A{}'(r_1) f_{1l}^B(r_1)}{m_A f_{1l}^A(r_1) f_{2l}^B{}'(r_1) - m_B f_{1l}^A{}'(r_1) f_{2l}^B(r_1)}, \tag{6}$$

where $F_l^C = [f_{1l}^C{}'(r_2) f_{2l}^C(R) - f_{l1}^C(R)\, f_{2l}^C{}'(r_2)]/[f_{1l}^C(r_2) f_{2l}^C(R) - f_{1l}^C(R)\, f_{2l}^C(r_2)]$ and the prime are used to denote the first radial derivative. From the condition of normalization $\int_0^R R_l^2(r)\, r^2\, dr = 1$ and the explicit form of functions *f*, we find A_1^l, $B_{1,2}^l$, $C_{1,2}^l$ and consequently the explicit analytical expressions for the normalized eigenfunctions. Explicitly values of functions *f* are given in Ref. [15].

2.3. Single-particle states by multi-band model within the k·p approach

The expansion of the envelope functions in terms of plane waves (see, e.g. Refs. [22, 23]) is one of the most used techniques within the **k·p** theory to obtain the energy structure of the nanostructures. By this method, Schrödinger's equation is solved by using Fourier transform of a superlattice formed by periodic boxes containing the nanostructure that is analysed. To avoid the artefacts induced by the artificial periodic boundary conditions imposed by the array of boxes, which can affect the accuracy of the results especially when Coulomb and/or strain field interactions are present, we consider a single nanostructure whose Hamiltonian is solved in a localized basis set defined over the volume of the nanostructure. Regarding the inner (core/shell interface) boundary conditions, we adopt the *weak* solution method (see, e.g. Lassen et al. [24]) and integrate over the whole volume of nanostructure to obtain matrix elements between basis states (formed by the products of envelope functions and zone-centre Bloch functions) for the Hamiltonian. This method is a convenient alternative to the method of imposing continuity of the envelope function and probability current at the core/shell interface to satisfy the boundary conditions. Details of computing the SPS energy structure by an eight-band model for CSQDs are given elsewhere [25].

2.4. Excitonic effect

To obtain an accurate description of the optical properties, in addition to the geometrical confinement and strain, the excitonic effect should be considered. In order of their contribution to the excitonic effect, the interactions that are commonly considered are as follows: the Cou-

lomb attractive interaction of the photoexcited electron-hole pair, the polarization interaction of the charges induced at the interfaces, the electron-hole exchange interactions and the correlation interactions [26, 27]. The polarization interaction, according to calculus of Brus [28], is about 3–5 times lower than the absolute value of Coulomb interaction and is smaller than the nanostructure size for ZnO, CdS, GaAs and InSb. The electron-hole exchange interaction is smaller. For example, in spherical InAs QDs of radius 3 nm, it is of 2.093 meV comparatively to the Coulomb interaction of 60.6 meV [26] and of order 0.1 meV in CdSe/CdS QD with thick shell [27]. The correlation interaction is also of order 1–2 meV or smaller [29]. For the level of accuracy of the two-band model introduced in Section 2.1, the Coulomb electron-hole interaction yields a reliable estimation of the excitonic effect. The muti-band **k·p** method is more accurate and, within this approach, calculus of all the above-mentioned interactions is possible at the desired accuracy.

Next, we limit discussion at modelling the excitonic effect by the Coulomb electron-hole interaction mediated by a *homogenized* dielectric constant (see below). We write the exciton state α as a configuration interaction expansion, $\left|\Psi^{(\alpha)}\right\rangle = \sum_{i,j=1} C_{ij}^{(\alpha)} c_i^+ h_j^+ |0\rangle$, with $|0\rangle$ the ground state (filled VB) and c_i^+ (h_i^+) as creation operator of the electron (hole) state $\psi_i^e(\mathbf{r}) = \langle \mathbf{r}|c_i^+|0\rangle$ ($\psi_i^h(\mathbf{r}) = \langle \mathbf{r}|h_i^+|0\rangle$). The excitonic spinless QD Hamiltonian formed by the kinetic part and Coulomb electron-hole interaction in the second quantization is written as [30]

$$H_D = \sum_m E_m^e c_m^+ c_m + \sum_m E_m^h h_m^+ h_m + \sum_{m,n,p,q} V_{mnpq}^{eh} c_m^+ h_n^+ h_p c_q, \tag{7}$$

where the first and second term stand for electron and hole kinetic energy, and the third for electron-hole Coulomb interaction, respectively. According to Maxwell Garnett (MG) formalism [31, 32] for spherical structures, the non-local dielectric constant may be replaced by a homogenized value, and will adopt this approach in our calculus. With the algebra of the second quantization, one obtains the secular equation:

$$\sum_{i,j,k,l=1} \left[\left(E_i^e + E_j^h - E \right) \delta_{ik} \delta_{jl} + V_{ijlk}^{eh} \right] C_{kl} = 0, \tag{8}$$

where $V_{i,j,k,l}^{eh} = -e^2 \left(4\pi\varepsilon_0 \bar{\varepsilon}_r\right)^{-1} \iint_V d\mathbf{r}_e d\mathbf{r}_h \psi_i^e(\mathbf{r}_e)^* \psi_j^h(\mathbf{r}_h)^* \left|\mathbf{r}_e - \mathbf{r}_h\right|^{-1} \psi_k^h(\mathbf{r}_h) \psi_l^e(\mathbf{r}_e)$ are Coulomb matrix elements and $\bar{\varepsilon}_r$ is the homogenized screened relative dielectric constant. In the concrete calculus of the Coulomb matrix elements, we used the series expansion of the Coulomb Green function in spherical harmonics

$$\frac{1}{\left|\mathbf{r}_e - \mathbf{r}_h\right|} = 4\pi \sum_{L=0}^{\infty} \sum_{m=-L}^{L} \frac{1}{2L+1} \frac{r_<^L}{r_>^{L+1}} Y_{Lm}^*(\hat{\mathbf{r}}_e) Y_{Lm}(\hat{\mathbf{r}}_h) \tag{9}$$

and the angular integrals separately factorize for electron and hole and they are computed analytically by using Gaunt's formula.

2.5. Optical absorption

In this section, we derive an expression of the absorption coefficient, which is valid in the limit of low-light irradiation power. We approximate the absorptive material as being formed by QDs in contact and assume that each QD is an absorber of volume V_{QD}. At the low-light irradiation power, the assumption of a linear relation between the polarization and the electric field is a common approximation. By treating the QD-field interaction as a perturbation, absorption coefficient expression can be obtained using either first-order complex susceptibility or Fermi's golden rule. Here, in the proof, we consider Fermi's golden rule as follows. For a monochromatic electromagnetic wave $\mathbf{E} = \mathbf{E}_0 \cos(\omega t - kz)$, propagating in z direction in a macroscopic non-conducting media, the gradient of the energy density is (see, e.g. Ref. [33]) $dw/dz = nc^{-1} dw/dt$. The loss of energy per time unit is the loss of energy in a *single* QD that is, $dw/dt = -\hbar\omega V_{QD}^{-1} R$, where R is the rate of change of the number of photons. From the last two equations, one obtains $dw/dz = -\hbar\omega R V_{QD}^{-1} nc^{-1}$. With the energy density $w = \varepsilon_r \varepsilon_0 E_0^2/2$, the intensity of the electromagnetic wave is (see Eqs. (7.13) (7.14) in Ref. [34]) $I = \sqrt{\varepsilon_r \varepsilon_0/(\mu_r \mu_0)} E_0^2/2 \approx c\varepsilon_0 \varepsilon_r E_0^2/(2n) = wc/n$, where $n = \sqrt{\mu_r \varepsilon_r} \cong \sqrt{\varepsilon_r}$ (Eq. (7.5) in Ref. [34]). Next, by combining the expressions of dw/dz, the derivative dI/dz and the Beer-Lambert law, $dI/dz = -\alpha_{QD} I$, we obtain the single QD absorption coefficient.

$$\alpha_{QD} = \frac{2\hbar\omega}{cn\varepsilon_0 E_0^2 V_{QD}} R. \tag{10}$$

Expression of the probability rate for absorption in the first order of approximation, R, can be obtained following the standard textbook derivation of Fermi's golden rule as

$$R = \frac{\pi e^2 E_0^2}{2 m_0^2 \hbar\omega^2} \sum_{i,f} \left| M_{if} \right|^2 \delta\left(E_{if} - \hbar\omega \right), \tag{11}$$

where $M_{if} = \left\langle \Psi_i \middle| \mathbf{e} \cdot \mathbf{P} \middle| \Psi_f \right\rangle$ is the optical matrix element between the initial $\left|\Psi_i\right\rangle$ and the final $\left|\Psi_f\right\rangle$ states, $E_{if} = \hbar\left(\omega_i - \omega_f\right)$, and δ is the Dirac function. To mimic the homogenous broadening that takes into account the relaxation phenomena of the carriers, one replaces the Dirac function by a Lorentzian of width γ, and the single QD absorption coefficient valid for low temperatures becomes.

$$\alpha_{QD} = \frac{e^2}{cn\varepsilon_0 m_0^2 \omega V_{QD}} \sum_{i,f} \frac{\gamma \left| M_{if} \right|^2}{\gamma^2 + \left(E_{if} - \hbar\omega \right)^2}. \tag{12}$$

Eq. (12) can be applied to obtain the excitonic absorption by computing the optical matrix element $M_{0\alpha} = \langle 0 | \mathbf{e} \cdot \mathbf{P} \left| \Psi^{(\alpha)} \right\rangle$, where **e** is the polarization light unit vector. Thus, by writing the transition linear momentum operator in the basis set $\left\{ |0\rangle, \left| \Psi^{(\alpha)} \right\rangle \right\}$ as $\mathbf{P} = \sum_\alpha |0\rangle\langle 0| \sum_{i=1}^{N} \mathbf{p}_i \left| \Psi^{(\alpha)} \right\rangle \left\langle \Psi^{(\alpha)} \right| + h.c.$, one obtains

$$M_{0\alpha} = \mathbf{e} \cdot \sum_{i,j,k=1} C_{ij}^{(\alpha)} \langle 0 | \mathbf{p}_k c_i^+ h_j^+ | 0 \rangle = \mathbf{e} \cdot \sum_{i,j=1} C_{ij}^{(\alpha)} \left\langle \psi_j^h u_v \left| \mathbf{p} \right| \psi_i^e u_c \right\rangle = \mathbf{e} \cdot \mathbf{p}_{vc} \sum_{i,j=1} C_{ij}^{(\alpha)} \left\langle \psi_j^h \left| \psi_i^e \right. \right\rangle, \tag{13}$$

where $\mathbf{p}_{vc} = \left\langle u_v \left| \mathbf{p} \right| u_c \right\rangle$; the last equality is obtained by making use of the slow spatial variation of the envelope wave functions over regions of the unit cell size and the orthonormality of the Bloch cell wave functions. By introducing the Kane momentum matrix element, $P = -i(\hbar/m_0)\langle s|p_z|z\rangle = -i(\hbar/m_0)\left\langle u_c \left| p_z \right| u_v \right\rangle = -i(\hbar/m_0) p_z^{cv}$, with $E_P = 2m_0 |P|^2/\hbar^2$ and considering the polarization unit vector, **e**, parallel to the quantization axis, *z*, for example, one obtains

$$\left| M_{0\alpha} \right|^2 = \frac{E_P m_0}{2} \left| \sum_{i,j=1} C_{ij}^{(\alpha)} \left\langle \psi_j^h \left| \psi_i^e \right. \right\rangle \right|^2. \tag{14}$$

Then, expression of the single QD absorption coefficient from Eq. (12) becomes

$$\alpha_{QD}(\omega) = \frac{\alpha_0}{\omega} \sum_{\tau} \left| \sum_{i,j=1} C_{ij}^{(\tau)} \left\langle \psi_i^e \left| \psi_j^h \right. \right\rangle \right|^2 \frac{\gamma}{\left(E_\tau - \hbar\omega \right)^2 + \gamma^2}, \tag{15}$$

where $\alpha_0 = e^2 E_P / \left(2nc\varepsilon_0 m_0 V_{QD} \right)$. The multi-shell character is brought into the excitonic optical matrix element,

$$f_{0\tau} = \left| \sum_{i,j=1} C_{ij}^{(\tau)} \left\langle \psi_i^e \left| \psi_j^h \right. \right\rangle \right|^2, \tag{16}$$

by the domain dependence of the electron and hole single SPSs. The quantity expressed by Eq. (15) is the exciton oscillator strength. For the exciton state at resonance, one obtains that the absorption coefficient is proportional to the exciton oscillator strength. As the parameters entering Eq. (15) characterizes a single QD, we name it *single* QD absorption coefficient. Neglecting light scattering, a good approximation for QD of small size comparatively to the light wavelength, we introduce a *colloidal* absorption coefficient for the measured absorption coefficient in experiment:

$$\alpha_{sol} = -c_{QD}^{1/3} \ln\left[1 - 4R^2 c_{QD}^{2/3}\left(1 - e^{-2R\,\alpha_{QD}}\right)\right], \tag{17}$$

where c_{QD} is the concentration of QDs in solution and ln is the natural logarithm function. The model is based on a probabilistic hitting QD as a target and details of the derivation can be found in Ref. [15]. For $\alpha_{QD}R << 1$ (that is QDs with radius smaller than approximately 10 nm) and $Rc_{QD}^{1/3} << 1$ (that is for dilute solutions), we obtain $\alpha_{sol} = 8R^3 c_{QD}\alpha_{QD}$.

3. Application of type I and II semiconductor heterostructures

In this section, we apply the theory developed in Section 2 to heterostructures of type I and II of direct band gap semiconductors. In accordance with our continuum model for strain, we consider QD structures with thicker shells. On the other hand, as a two-band model neglects both VB-CB and VB sub-band mixing, we assess its validity in our modelling. As a first requirement in neglecting VB-CB mixing, the semiconductors should be of wide enough band gap. Regarding neglecting of the VB sub-band mixing, things are more complicated, and to assess to what extent a two-band model respects a specific accuracy, a more advanced theoretical treatment is necessary. For this purpose, we compare the SPSs generated by the two- and eight-band approaches for CSQDs of wide band gap semiconductors. For the modelling, we consider ZnTe/ZnSe CSQD (a type II heterostructure), ZnTe/ZnSe/ZnS CSS QD (a type II ZnS-coated heterostructure) and CdSe/CdS/ZnS CSS QD (a type I ZnS-coated heterostructure).

3.1. Comparison of two- and eight-band approaches for wide band gap CSQDs

Before focusing discussion on quantum mechanics calculation of SPSs, we apply our method of computing the strain in lattice-mismatch heterostructures. The results obtained by solving Eqs. (1) for the general case of different elastic parameters presented in **Figure 1** for CdSe/11CdS/ZnS (CSS QDI) and ZnTe/16ZnSe/ZnS (CSS QDII); the numbers before the chemical symbols hold for the number of MLs and the core radii are of 2 nm and 2.2 nm, respectively.

The parameters we use are listed in **Table 1**.

Once the hydrostatic strain and the bulk band offset are known, we can obtain the band lineup in the presence of the strain, by using Eq. (2). The bulk energy structure of the heterostructures

(band offset) we discuss is schematically shown in **Figure 2** for CdSe/CdS/ZnS and ZnTe/ZnSe/ZnS (in what follows we take as zero reference the bulk VB edge of the core semiconductor).

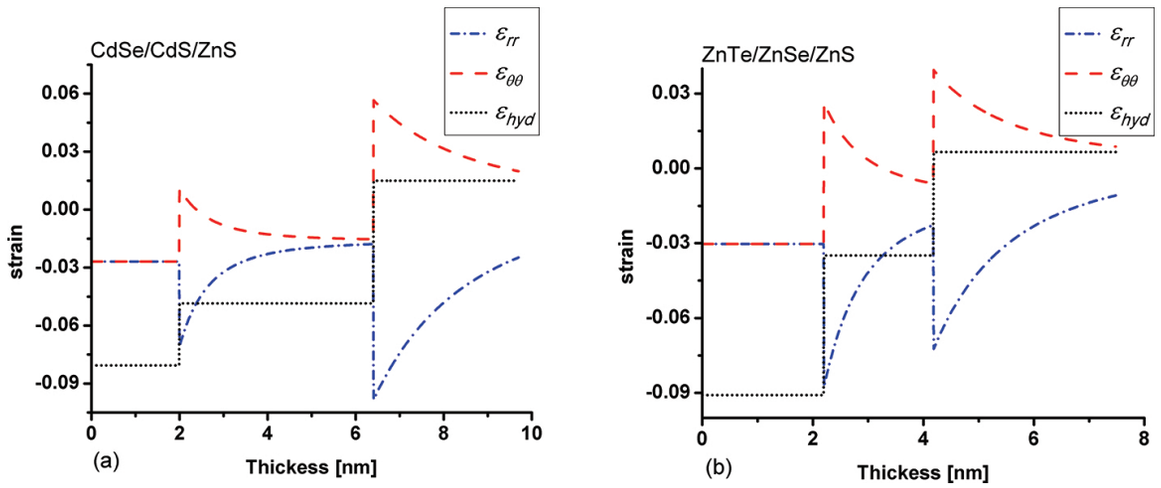

Figure 1. Diagonal spherical tensor components, ε_{rr}, $\varepsilon_{\theta\theta}$, $\varepsilon_{\varphi\varphi}$ for (a) CdSe/11CdS/ZnS; (b) ZnTe/16ZnSe/ZnS for outer shell thickness of 3.3 nm.

	ZnTe	**ZnSe**	**CdSe**	**CdS**	**ZnS**
a (Å)	6.08[a]	5.65[a]	6.05[b]	5.82[b]	5.40[c]
E (10^{10} N m^{-2})	4.17[a]	4.51[a]	2.87[d]	3.26[d]	5.55[c]
ν	0.363[a]	0.376[a]	0.408[d]	0.410[d]	0.384[c]
E_{gap} (eV)	2.25 [e]	2.69 [e]	1.74[e]	2.49[e]	3.61 [e]
E_v (eV)	-5.34 [e]	-6.07 [e]	-6.00 [e]	-6.42 [e]	-6.6 [e]
a_v (eV)	0.79[f]	1.65[f]	0.9[b]	0.4[b]	2.31[f]
a_c (eV)	-5.83[f]	-4.17[f]	-2.00[b]	-2.54[b]	-4.09[f]
γ_1	3.74[g]	3.77[g]	3.33[h]	4.11[d]	2.54[g]
γ_2	1.07[g]	1.24[g]	1.11[h]	0.77[d]	0.75[g]
γ_3	1.64[g]	1.67[g]	1.11[h]	1.53[d]	1.09[g]
m^{lh_i}	0.152	0.148	0.18	0.15	0.225
m^{hh_i}	1.092	1.292	0.90	0.60	1.582
m^{el}	0.20[j]	0.21[j]	0.15[k]	0.22[k]	0.34[l]
ε^m	7.4	9.1	10	8.9	9

[a]Ref. [35].
[b]Ref. [36].
[c]Ref. [37].
[d]Ref. [38].
[e]Ref. [39].

[f]Ref. [40].
[g]Ref. [41].
[h]Ref. [42].
[i]Calculated with $m^{hh/lh} = m_0\gamma_1^{-1}\left[1 \pm \left(6\gamma_3 + 4\gamma_2\right)/\left(5\gamma_1\right)\right]^{-1}$ from Ref. [43].
[j]Ref. [44].
[k]Ref. [45].
[l]Ref. [46].
[m]Ref. [47].
For 1 ML of ZnSe, we considered the thickness of 0.33 nm [48], and for 1 ML of ZnS, we approximated it as 0.33 nm also.

Table 1. Material parameters used in the work

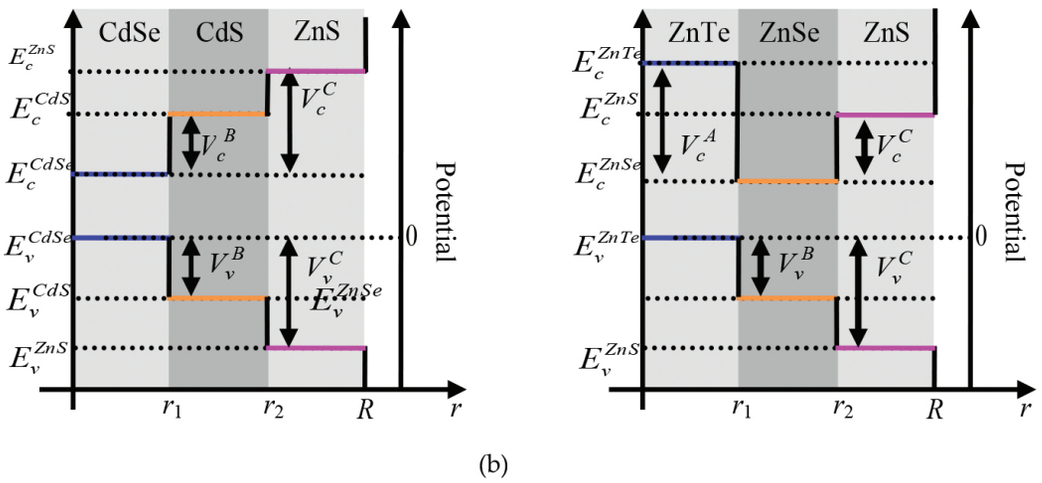

Figure 2. Schematic band lineups in CSS QDs for (a) CdSe/CdS/ZnS; (b) for ZnTe/ZnSe/ZnS heterostructures.

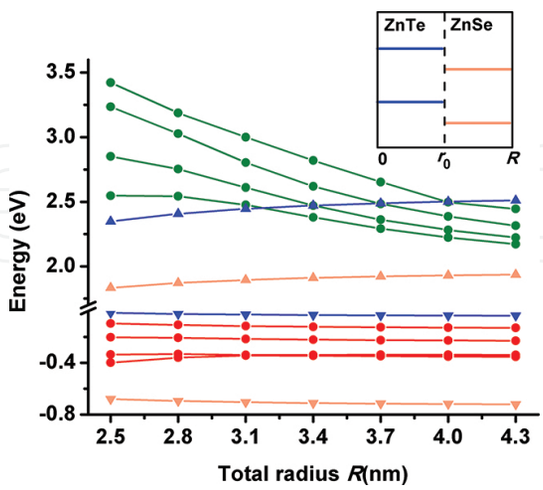

Figure 3. Energy of the first four electron (green colour) and hole (red colour) SPSs in ZnTe/ZnSe CSQDs of core radius 2.2 nm and variable total radius R in a two-band model. Continuum lines with up (down) triangle symbols show the band lineup in presence of lattice-mismatch strain of electron (hole) states for ZnTe (orange colour) and ZnSe (blue colour). The inset is for the lineup guidance. Zero reference is the bulk ZnTe VB edge.

Next, we discuss the SPSs obtained for ZnTe/ZnSe CSQDs by the two-band model introduced in Section 2. After calculus of the hydrostatic strain (by the method we mentioned above), we calculate the band lineup in the presence of the strain. For this, the bulk band offset assumed by Eq. (2) is take from Ref. [39]. To obtain the SPS structures, we take the version of Eqs. (5) and (6) for core/shell structure (see, for example, Ref. [16]). The eigenvalues of several electron and hole SPSs are presented in **Figure 3**. For a core radius of 2.2 nm, beginning with shell thicker than 3.1 nm, the lowest electron states start to be located in the shell while the highest hole states are practically insensitive to the shell thickness and located in the core. Our calculus shows that the first two or three (for shell thinner than 3.1 nm) hole SPSs are of heavy hole type.

To get a more complete image, in **Figure 4**, the probability density (PD) $\left|\psi_{nlm}(\mathbf{r})\right|^2$ is presented for a shell thickness of 4.3 nm. The SPSs energetically predicted location by the calculus of the eigenvalues is confirmed (checked) by the geometrical location. The degeneracy of the states is dictated by the angular momentum quantum number L and the PD shape by the values of n, L and $|m|$ (which results from the $Y_l^m(\theta,\varphi)$ dependence of the state).

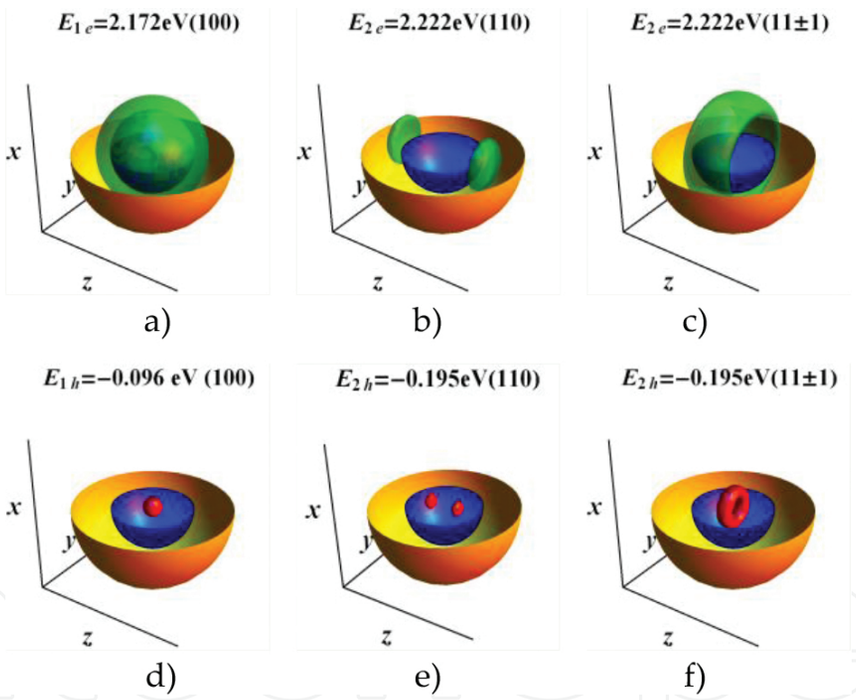

Figure 4. Two-band electron (green colour) and hole (red colour) SPS probability density $0.75 \times \max(\left|\psi_{nlm}(\mathbf{r})\right|^2)$ for ZnTe/ZnSe with core radius 2.2 nm and shell thickness 4.3 nm. The quantum numbers shown in the parentheses are, in order, n, L and m.

For comparison, we make several remarks on the SPS structure we obtained (see Ref. [25]) by the **k·p** method. According to the irreducible representations of T_d point group, the maximum value of degeneracy is four. Absent in the two-band model, the time-reversal symmetry is present in the eight-band model, and all SPSs are at least two-fold degenerate (Kramers degeneracy). The cubic symmetry of the zinc blende structures can also be observed in the PD

shape. The shape of the PD, except the mentioned cubic symmetry, is similar in the two approaches. To have a more complete image of the density of states in the two approaches, we collect and compare the eigenvalue for CSQDs of different shell thicknesses. One obtains that the density of states is larger in the eight-band model, and for these wide band semiconductors, this is mainly caused by the VB sub-band mixing. However, when the shell thickness increase, the CB SPSs become denser and the discrepancy decreases. Consistently, in both approaches, one obtains the red shift of the SPS fundamental inter-band transition with the shell thickness. The conclusion of the comparison is that if only several excited states are sufficient to be taken into account in modelling, then CSQDs with thicker shells and larger cores can be approximately characterized by a two-band model. Generally, the VB SPSs are a mixture of heavy, light and split-off hole states. The two-band calculus shows, as expected, that the close to the VB edge, the SPSs are heavy hole state type, and this is another approximation that can be used in a two-band modelling of this type of CSQDs. On another hand, in case higher excited states are necessary in modelling, then a two-band model becomes inadequate. We can compare our two-band model prediction with the experimental measurement of the fundamental absorption for this type of CSQDs with shell thickness of 5 ML. Thus, for core radius of 2.2 nm and total radius of 3.85 nm (corresponding approximately to 5ML ZnSe shell thickness), we obtain a transition of 517 nm (2.397 eV) comparatively to approximately 550 nm (2.254 eV) reported in Ref. [49]. Energy overestimation by our prediction is mainly due to neglecting of the excitonic effect. If we estimate the excitonic effect (binding energy) by an attractive interaction of 0.13 eV, then our prediction becomes 547 nm, close to the experiment. In the next section, we obtain an estimation of the binding energy from the calculus of the Coulomb electron-hole attraction.

3.2. Excitonic effect and optical absorption

In this section, we evaluate the excitonic effect for CSS QDI and CSS QDII with thick outer shell. First, following the model from the previous section, by using Eqs. (1), (2), (5) and (6), we obtain the SPS structure. In the calculations, for the both nanostructure types, we find that the first four VB SPS states are heavy hole states and the fifth is the first light hole. Since the density of states is higher for heavy hole states, according to discussion from the previous section, we can appreciate that a two-level approach is at least satisfactory if only the first several hole levels are taken into account in the modelling. The characteristics of the SPS structure are as follows. The red shift of the fundamental inter-band transition with the middle shell thickness is found. The optical stability effect of the outer shell as reported by experiment [7, 49] is explained by the slight variation of the SPS energy with the ZnS shell thickness. Both electron and hole are located in the core for CSS QDI while for CSS QDII, the hole is located in the core and the electron in the shell, revealing the type I and type II character of the heterostructures, respectively. These observations are shown in **Figure 5** (reproduced from Ref. [15]). The PDs for the SPSs can be seen in Ref. [15]. With the SPS structure obtained, we estimate the exciton binding energy (or in an equivalent formulation, the fundamental excitonic absorption (FEA)) by computing the Coulomb electron-hole attractive interaction by a configuration interaction method as introduced in Section 2.4. With the first four energy levels we consider, we form for both modelled nanostructures the set of

configurations as follows. The SPSs have the quantum numbers (n, L) = (1, 0), (2, 1), (3, 2) and (4, 3) for electron and (4, 0) for hole, and each state is $2L$+1 degenerated. Then, we build the configurations by replacing one from the set of (1 + 3 + 5 + 1) VB states with one of the (1 + 3 + 5 + 7) CB states, and obtain a total of 160 configurations.

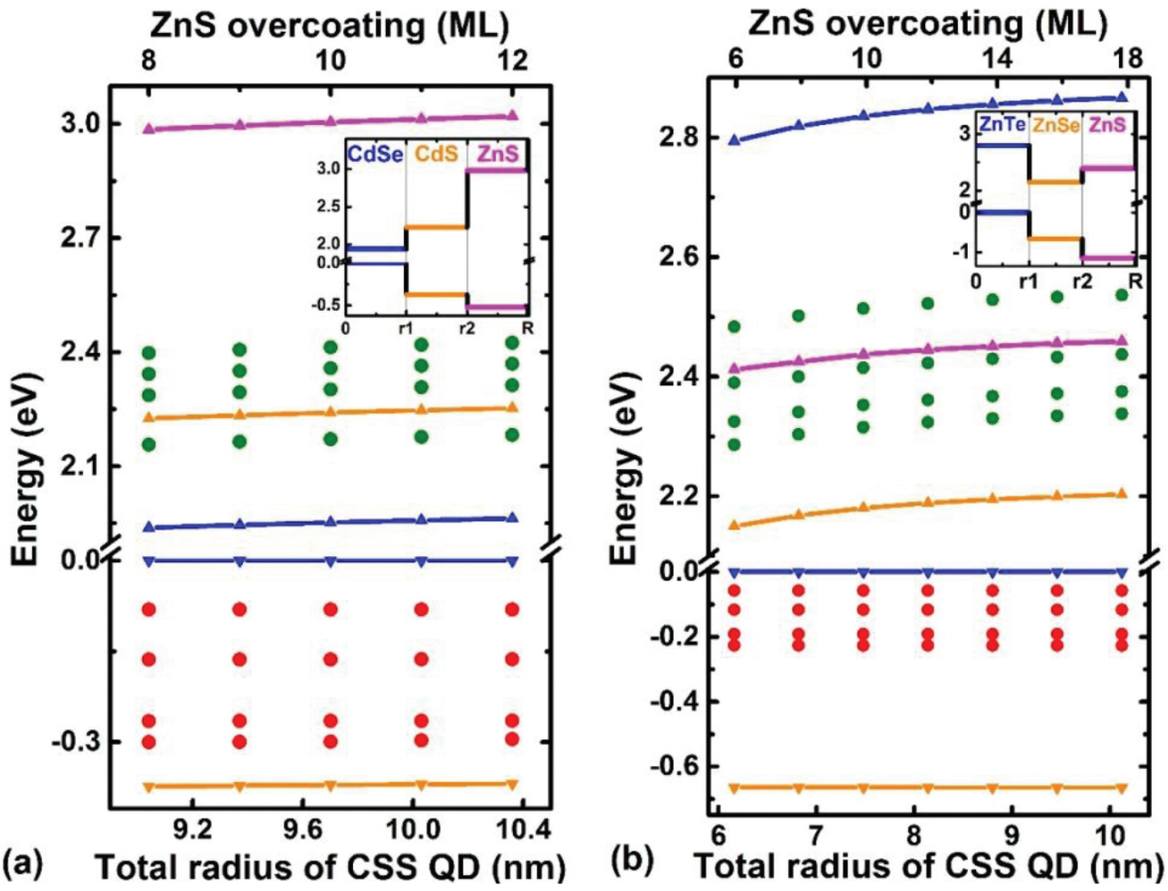

Figure 5. Energy of the first four electron (green colour) and hole (red colour) SPSs in (a) CSS QDI; (b) CSS QDII of total radius R. Continuum lines with up (down) triangle symbols show the band lineup in the presence of lattice-mismatch strain of electron (hole) states for ZnTe (blue colour), ZnSe (orange colour), ZnS (violet colour) in figure (a) and for CdSe (blue colour), CdS (orange colour), ZnS (violet colour) in figure (b). The insets are for the lineup guidance. Zero reference is core VB edge.

In **Figure 6** (reproduced from Ref. [15]), we show the energy value of FEA, E_{FEA}, the single QD absorption coefficient for the corresponding FEA (obtained by Eq. (15)), $\alpha_{FEA}(x)$ and the colloidal absorption coefficient for the corresponding FEA (obtained by Eq. (17)) $\alpha_{sol}(x)$; the argument x represents the number of ZnS-coating MLs. For the Kane energy, which is a necessary ingredient, we estimate $E_P = 20.4\mathrm{eV}$ for CSS QDI and $E_P = 19.1\mathrm{eV}$ for CSS QDII from Ref. [36]. Another necessary parameter is the CdS ML thickness, which we take as 0.4 nm, in accord with Ref. [27]. For **Figure 6(a)**, first, we setup the screened dielectric constant that is used to obtain the Coulomb matrix elements. Thus, we fit the experimental E_{FEA} of 620 nm from experiment [7] for CdSe/19CdS (CSQD with core radius of 2 nm and CdS shell thickness of 19

http://dx.doi.org/10.5772/65091

ML). Then, we analyse the effect of the ZnS coating and obtain the following results. E_{FEA} is slightly blue shifted with ZnS thickness and asymptotically blue shifted with the ZnS overcoating. Thus, a relative weak change of E_{FEA} with the ZnS overcoating as reported by the experiment [7] is obtained. This behaviour is primarily the result of the lattice-mismatch strain and secondly of the excitonic effect. $\alpha_{FEA}(x)$ obtained is asymptotically decreasing with ZnS coating. On another hand, the value obtained by the experiment, $\alpha_{sol}(x)$, is weakly changed by ZnS coating for 100 μM concentration of the colloidal QD solution. This is in agreement with the reported optical stability of such overcoated QDs [7] and with the slow variation of SPSs mentioned above. Also, from Eq. (15) we obtain that for $0 \rightarrow X_g$ transition corresponding to FEA, f_{0X_g} is very slightly varying with the ZnS coating. In a similar manner, we obtained **Figure 6(b)** as follows. First, to set-up the screened dielectric constant, we fit the experimental E_{FEA} for ZnTe/6ZnSe (CSQD with core radius of 2.2 nm and ZnSe shell thickness of 6ML) of 570 nm from experiment [49]. Then, we analyse the effect of the ZnS coating and obtain the following results.E_{FEA} is weakly blue shifted with the ZnS overcoating as reported by the experiment [49]. Differently from the CSS QDI, the single QD absorption coefficient is decreasing by one order of magnitude with ZnS coating. This is the result of the orbitals overlap decreasing with the ZnS coating, the electron is more pronouncedly shifted to the outer shell. We obtain that α_{sol} also strongly decreases with the ZnS coating but as in the type I case, it is almost constant with the ZnS overcoating. This dependence can be related to the protecting effect of the ZnS overcoating reported by experiment [49]. From Eq. (15), we obtain f_{0X_g} decreases about five times by ZnS coating and is weakly sensitive with the ZnSovercoating.

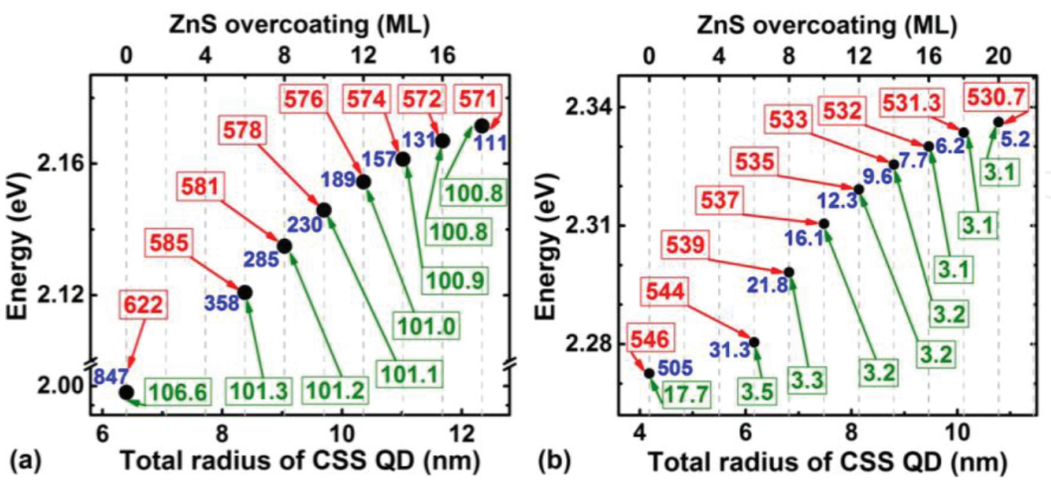

Figure 6. FEA (black circle and red-bordered label for the energy expressed in units of nm), α_{FEA} (blue label, units of $10\mathrm{cm}^{-1}$), α_{sol} (green, bordered label, units of $0.01\mathrm{cm}^{-1}$) for (a) CdSe/11CdS/xZnS QD; (b) ZnTe/6ZnSe/xZnS QD. α_{sol} is obtained for 100 μM concentration of the colloidal QD solution.

Regarding the location of the photoexcited charges, we introduce the radial probability density $D_{\alpha}^{(Xg)}(r) = \sum_{i,j}\left|C_{ij}^{(Xg)}\right|^2 r^2 \int \left|\psi_i^{\alpha}(\mathbf{r})\right|^2 d\Omega$, where $\alpha = e,\ h$ for electron and hole, respectively. One observes that $\int_0^R D_{\alpha}^{(Xg)}(r)\, dr = 1$ since $\sum_{i,\ j}\left|C_{ij}^{(Xg)}\right|^2 = 1$ from the orthonormalization condition. The radius expectation value of the photoexcited electron or hole is obtained with $\overline{r_{\alpha}^{(Xg)}} = \sum_{i,j}\left|C_{ij}^{(Xg)}\right|^2 \langle\psi_i^{\alpha}|r|\psi_i^{\alpha}\rangle$. The results are remarkable by revealing the ZnS coating effect. Thus, coating is not significant for CSS QDI, the electron and hole remain located in the core not close to the core/shell interface. On the other hand, for CSS QDII, the hole radius expectation value is practically not affected by the ZnS coating and the hole remains close to the centre but the ZnS coating has a strong effect on the electron localization, namely, the electron moves to the middle of the ZnSe shell. Numerical details are given in (Ref. [15]). Thus, according to our modelling in both CSS QDI and CSS QDII, the electron and hole are not confined in the proximity of the interfaces and surface. Consequently, QD coating induces larger photoexcited carrier-trap (interface defects and impurities close to the core/shell interface or to the outer-shell-environment interface) separation. This might have an important effect regarding the competition between recombination and trapping. Thus, one of the interesting effects of the QD coating is the blinking suppression observed, for example, in ultra-thick-shell CdSe/CdS [50]. According to our results, the model assuming a tunnelling barrier between the photoexcited carriers and the trap states, similar to that proposed in Ref. [51] can simplely explain the non-blinking as follows. Coating induces increasing of the barrier thickness and consequently a lowering of the trapping probability. Then, under a continuous photoexcitation, (stimulated) recombination is more probable than the trapping and a continuous luminescence (non-blinking) is observed from coated QDs. Given the low trapping probability heuristically concluded by our modelling, for the non-bliking in coated QDs, we rather advocate the barrier model than the model of Auger recombination of the photoexcited carriers on the trapping states as proposed in Ref. [50].

4. Conclusions

We described optical properties of CSQDs of type I and II with thick shells by a two-band model, which first is justified by a comparison with an eight-band **k·p** model. To obtain the lattice-mismatch strain effect on the energy structure, we developed a continuum elasticity model for isotropic, homogeneous and finite size multi-layer structures. When implemented in the specific quantum mechanics of the multi-shell semiconductor nanocrystals, the strain model we introduce is able to predict the main characteristics of fundamental absorption in thick shell CSQDs. By taking into account the excitonic effect, we can explain the optical stability of the overcoated core/shell QDs. According to our estimations, the measured absorption coefficient in colloidal QD solutions is practically not sensitive to the overcoating. The most important finding regarding the coating effect is related to the photoexcited carrier

localization. According to our predictions, the photoexcited carriers are moved away from the surface and interfaces by overcoating. We believe that this work is an argument for improving the modelling. An eight-band treatment able to describe the optical absorption of ZnTe/ZnSe CSQDs which considers high excited states is already done (see Ref. [25]). In this context, the analysis of the multi-exciton generation, electron-phonon interaction and relaxation dynamics are promising successful directions of research in finding responses to the complex optical processes that take place in multi-layer QDs.

Author details

Tiberius O. Cheche

Address all correspondence to: cheche@gate.sinica.edu.tw

Faculty of Physics, University of Bucharest, Bucharest, Romania

References

[1] Kamat PV. Quantum dot solar cells. The next big thing in photovoltaics. The Journal of Physical Chemistry Letters. 2012;4:908–918.

[2] Chen Y, Herrnsdorf J, Guilhabert B, Zhang Y, Watson IM, Gu E, Laurand N, Dawson MD. Colloidal quantum dot random laser. Optics Express. 2011;19(4):2996–3003.

[3] Kairdolf BA, Smith AM, Stokes TH, Wang MD, Young AN, Nie S. Semiconductor quantum dots for bioimaging and biodiagnostic applications. Annual Review of Analytical Chemistry (Palo Alto Calif). 2013;6:143–162.

[4] Dietl T. Exchange interactions and nanoscale phase separations in magnetically doped semiconductors. In: Dietl T, Awschalom DD, Kaminska M, Ohno H, editors. Spintronics, Semiconductors and Semimetals. Vol 82. 1st ed. USA: Academic Press; 2008. pp. 371–412.

[5] Trotta R, Zallo E, Ortix C, Atkinson P, Plumhof D, van den Brink J, Rastelli A, Schmidt OG. Universal recovery of the energy-level degeneracy of bright excitons in InGaAs quantum dots without a structure symmetry. Physical Review Letters. 2012;109(14): 147401(1–4).

[6] García-Santamaría F, Chen Y, Vela J, Schaller RD, Jennifer A, Hollingsworth JA, Klimov V. Suppressed auger recombination in "giant" nanocrystals boosts optical gain performance. Nano Letters. 2009;9(10):3482–3488.

[7] Chen Y, Vela J, Htoon H, Casson JL, Donald J, Werder DJ et al. "Giant" multishell CdSe nanocrystal quantum dots with suppressed blinking. Journal of the American Chemical Society. 2008;130(15):5026–5027.

[8] Gronqvist J, Sondergaard N, Boxberg F, Guhr T, Aberg S, Xu HQ. Strain fields in core-shell nanowires. Journal of Applied Physics. 2009;106:053508.

[9] Sarkar P, Springborg M, Seifert G. A theoretical study of the structural and electronic properties of CdSe/CdS and CdS/CdSe core/shell nanoparticles. Chemical Physics Letters. 2005;405:103–107.

[10] Li JB, Wang LW. First principle study of core/shell structure quantum dots. Applied Physics Letters. 2004;84(18):3648–3650.

[11] Yang SY, Prendergast D, Neaton JB. Strain-induced band gap modification in coherent core/shell nanostructures. Nano Letters. 2010;10:3156–3162.

[12] Pryor C, Kim J, Wang LW, Williamson J, Zunger A. Comparison of two methods for describing the strain profiles in quantum dots. Journal of Applied Physics. 2009;106(5): 2548–2554.

[13] Ma HM, Gao XL. Strain gradient solution for a finite-domain Eshelby-type plane strain inclusion problem and Eshelby's tensor for a cylindrical inclusion in a finite elastic matrix. International Journal of Solids and Structures. 2011;48:44–55.

[14] Landau LD, Lifshitz EM. Theory of elasticity. Bristol. Pergamon. 1970.

[15] Pahomi TE, Cheche TO. Strain influence on optical absorption of giant semiconductor colloidal quantum dots. Chemical Physics Letters. 2014;612:33–38.

[16] Cheche TO, Barna V, Chang YC. Analytical approach for type-II semiconductor spherical core–shell quantum dots heterostructures with wide band gaps. Superlattice and Microstructures. 2013;60:475–486.

[17] Grundmann M, Stier O, Bimberg D. InAs/GaAs pyramidal quantum dots: Strain distribution, optical phonons, and electronic structure. Physical Review B. 1995;52(16): 11969–11981.

[18] Van de Walle CG. Band structure of indium antimonide. Journal of Physics and Chemistry of Solids. 1989;39(4):1871–1883.

[19] Kane EO. Band structure of indium antimonide. Journal of Physics and Chemistry of Solids. 1957;1(4):249–261.

[20] Bir GL, Pikus GE. Symmetry and Strain-Induced Effects in Semiconductors. New York: Wiley; 1975.

[21] Bahder TB. Eight-band k.p model of strained zinc-blende crystals. Physical Review B. 1990;41(17):11992–12001.

[22] Baraff GA, Gershoni D. Eigenfunction-expansion method for solving quantum-wire problem: Formulation. Physical Review B. 1991;43(5):4011–4022.

[23] Gershoni D, Henry CH, Baraff GA. Calculating the optical properties of multidimensional heterostructures: application to the modeling of quatemary quantum well lasers. IEEE Journal of Quantum Electronics. 1993;29(9):2433–2450.

[24] Lassen B, Lew Yan Voon LC, Willatzen M, Melnik R. Exact envelope-function theory versus symmetrized Hamiltonian for quantum wires: a comparison. Solid State Communications. 2004;132:141–149.

[25] Cheche TO, Chang YC, Barna V. CMD-24, Abstract Book. Discretized total angular momentum basis within eight-band k.p theory: application to heteroepitaxial core-shell quantum dots. [Internet]. September 2012 . Available from: http://www.cmd-24.org/home.

[26] Luo JW, Bester G, Zunger A. Long- and short-range electron–hole exchange interaction in different types of quantum dots. New Journal of Physics. 2009;11:123024.

[27] Brovelli S, Schaller RD, Crooker SA, Garcia-Santamaria G, Chen Y, Viswanatha R et al. Nano-engineered electron–hole exchange interaction controls exciton dynamics in core–shell semiconductor nanocrystals. Nature Communications. 2011;2(280):1-8. DOI: 10.1038/ncomms1281

[28] Brus LE. Electron–electron and electron–hole interactions in small semiconductor crystallites: the size dependence of the lowest excited electronic state. Journal of Chemical Physics. 1989;80(9):4403–4409.

[29] Shumway J, Franceschetti A, Zunger A. Correlation versus mean-field contributions to excitons, multiexcitons, and charging energies in semiconductor quantum dots. Physical Review B. 2001;63:155316 1–13.

[30] Hawrylak P. Excitonic artificial atoms: Engineering optical properties of quantum dots. Physical Review B. 1999;60:5597–5608.

[31] Garnett JCM. Colours in metal glasses and in metallic films. Philosophical Transactions of the Royal Society A. 1904;203:385–420.

[32] Holmström P, Thylén L, Bratkovsky A. Dielectric function of quantum dots in the strong confinement regime. Journal of Applied Physics. 2010;107:064307(1–7).

[33] Mitin V, Kochelap V, Stroscio MA. Quantum Heterostructures: Microelectronics and Optoelectronics. 1st ed. Cambridge: Cambridge University Press; 1999.

[34] Jackson JD. Classical Electrodynamics. 3rd ed. New York: John Wiley and Sons; 1999.

[35] Berlincourt D, Jaffe H, Shiozawa LR. Electroelastic properties of the sulfides, selenides, and tellurides of zinc and cadmium. Physical Review. 1963;129:1009.

[36] Li YH, Gong XG, Wei SH. Ab initio all-electron calculation of absolute volume deformation potentials of IV–IV, III–V, and II–VI semiconductors: the chemical trends. Physical Review B. 2006;73:245206(1–5).

[37] Hall RB, Meakin JD. The design and fabrication of high efficiency thin film CdS/Cu2S solar cells. Thin Solid Films. 1979;63(1):203–211.

[38] Adachi S. Properties of Group-IV, III-V and II-VI Semiconductors. Chichester: John Wiley and Sons; 2005.

[39] Lo SS, Mirkovic T, Chuang CH, Burda C, Scholes GD. Emergent properties resulting from type-II band. Advanced Materials. 2010;XX:1–18.

[40] Van de Walle CG. Band lineups and deformation potentials in the model-solid theory. Physical Review B. 1989;39(3):1871.

[41] Lawaetz P. Valence-band parameters in cubic semiconductors. Physical Review B. 1971;4(19):3460–3467.

[42] Mourad D, Richters JP, Gerard L, Andre R, Bleuse J, Mariette H. Determination of the valence band offset at cubic CdSe/ZnTe type II heterojunctions: a combined experimental and theoretical approach [Internet]. Available from: arXiv:1208.2188v2

[43] Baldereschi A, Lipari NO. Spherical model of shallow acceptor states in semiconductors. Physical Review B. 1979;8(6):2697–2709.

[44] Singh J. Physics of Semiconductors and Their Heterostructures. New York: McGraw-Hill; 1993.

[45] Singh J. Semiconductor Optoelectronics: Physics and Technology. New York: McGraw-Hill; 1995.

[46] Barman B, Sarma KC. Luminescence properties of ZnS quantum dots embedded in polymer matrix.Chalcogenide Letters. 2011;8(3):171–176.

[47] Palmer DW. The Semiconductors-information [Internet]. 2008 03 . Available from: www.semiconductors.co.uk

[48] Smith AM, Mohs AM, Nie S. Tuning the optical and electronic properties of colloidal nanocrystals by lattice strain. Nature Nanotechnology. 2009;4(1):56–63.

[49] Bang J, Park J, Lee JH, Won N, Nam J. ZnTe/ZnSe (core/shell) type-II quantum dots: Their optical and photovoltaic properties. Chemistry of Materials. 2010;22(1):233–240.

[50] Galland C, Ghosh Y, Steinbruck A, Hollingsworth JA, Htoon H, Klimov VI. Lifetime blinking in nonblinking nanocrystal quantum dots. Nature Communications. 2012;3(908):1–7. DOI: 10.1038/ncomms1916

[51] Kuno M, Fromm DP, Hamann HF, Gallagher A, Nesbitt DJ. Nonexponential "blinking" kinetics of single CdSe quantum dots: a universal power law behavior. Journal of Chemical Physics. 2000;112(7):3117–3120.